Chain vol. X, no. X, pp. 1–XX, 202X
DOI:10.23919/CHAIN.2026.000006
ISSN 2097-3470
CN 10-1915/TB
Research Article

Fluorinated MOF-enabled flexible triboelectric system with integrated energy harvesting and storage

Jing Liu[1], Dong Wang[1], Dingyi Yang[1], Yong Wang[2], Yizhang Wu[3,✉], and Yongmei Wang[1,✉]

[1] *School of Physics, School of Advanced Materials and Nanotechnology, Xidian University, Xi'an 710126, China*
[2] *Academy of Advanced Interdisciplinary Research, Faculty of Integrated Circuits, Xidian University, Xi'an 710071, China*
[3] *Department of Applied Physical Sciences, The University of North Carolina at Chapel Hill, Chapel Hill, NC 27514, USA*

Received: 9 January 2026
Revised: 2 February 2026
Accepted: 9 February 2026

KEYWORDS

metal-organic framework,
supercapacitor,
self-powered systems,
triboelectric
nanogenerator,
UiO-66-4F

ABSTRACT

Triboelectric nanogenerators (TENGs) are constrained by the inherent material limitations and systemic performance bottlenecks. Conventional polydimethylsiloxane (PDMS) triboelectric layers offer limited control over surface electronegativity, interfacial polarization, and charge retention, hindering stable self-powered operation. To address these challenges, we report a flexible triboelectric system based on a fluorinated metal-organic framework (MOF), UiO-66-4F, which integrates energy harvesting and storage via coordinated design across materials, devices, and circuits. The triboelectric nanogenerator (UF-TENG), fabricated from a UiO-66-4F@PDMS composite layer with 10 wt% filler, generates an open-circuit voltage of 180 V and a short-circuit current of 11 μA, representing 3- and 1.83-fold enhancements over pristine PDMS. The UF-TENG also exhibits stable output over 10,000 cycles under 20% tensile strain. The flexible supercapacitor incorporating 20 wt% UiO-66-4F/LiCl exhibits lower high-frequency impedance and near-ideal low-frequency phase angle, and has typical double-layer capacitance characteristics for efficient charge management. The output-voltage fluctuation of the integrated device is 60% lower than that of a separate TENG, maintaining a stable output for 4,500 s, effectively improving power storage and output stability. This work demonstrates that functional group engineering in MOFs not only enhances triboelectric charge generation but also facilitates efficient charge management, offering a compact, durable, and integrable power solution for wearable electronics.

Address correspondence to Yizhang Wu, yizhwu@unc.edu; Yong-Mei Wang, wangym1001@xidian.edu.cn

1 Introduction

With the rapid advancement of wearable electronics and the distributed Internet of Things (IoT), there is an increasing demand for lightweight, flexible power supplies that can operate stably under low-frequency and intermittent excitation conditions [1–4]. However, the sustainable development of such devices is limited by the existing power supply system [5]. Conventional rigid batteries struggle to combine flexibility with high energy density, limiting their applicability in flexible and wearable electronics [6]. In contrast, emerging energy-harvesting technologies such as triboelectric nanogenerators (TENGs) can efficiently harness mechanical energy from the environment, yet ensuring a stable and continuous power output remains a critical bottleneck [7]. TENGs are capable of generating high voltages and large amounts of charge. Still, their low currents and erratic power levels make them challenging to use in a wide range of commercial applications. Therefore, it is essential to combine them with energy storage devices [8]. The integration of TENGs with supercapacitors (SCs) presents a promising strategy for constructing self-powered systems. However, the performance of this integrated system is often limited by fundamental mismatch problems at the material level. Conventional polymer friction layers face inherent limitations in surface electronegativity and charge-retention capability [9]. Meanwhile, the dielectric layers in solid-state SCs generally suffer from low ionic conductivity and a mismatch with the pulsed output characteristics of TENGs. Therefore, developing multifunctional materials that can simultaneously enhance triboelectric charge generation and optimize ion transport is crucial for advancing integrated self-powered systems.

In flexible TENGs, the selection of the triboelectric layer material directly affects the energy conversion efficiency. TENGs convert mechanical energy into electrical energy through the synergistic effects of the electrode and the triboelectric layer, contact electrification, and electrostatic induction. However, the ultimate output performance is directly influenced by the charge induction and trapping abilities of the triboelectric material [8, 10]. Polydimethylsiloxane (PDMS) has emerged as a predominant material for the negative triboelectric layer in TENGs, owing to its flexibility, chemical inertness, and low cost [11, 12]. Nevertheless, the intrinsically low dielectric constant and high insulation properties of PDMS restrict its charge storage capacity and overall power output. To address this limitation, incorporating high-dielectric-constant or charge-trap fillers into the PDMS matrix has become a widely adopted strategy [13–15]. Yang et al. [16] employed graphene oxide (GO) to modify the porous PDMS friction layer, resulting in a significant enhancement in the performance of TENGs, with the output voltage and current increasing by factors of 2.89 and 4.18, respectively. In another approach, strontium-doped barium titanate was employed as an active filler in PDMS, effectively enhancing triboelectric performance through a synergistic mechanism that combines an elevated dielectric constant with enhanced charge-trapping capability [11, 17–19].

Metal-organic framework (MOF) materials offer promising avenues for optimizing the properties of friction layers, owing to their high specific surface area, tunable chemical structures, and strong electronegativity [20, 21]. As a typical class of zirconium-based frameworks, the UiO-66 series exhibits excellent chemical stability and tunability. Functional group modification, such as fluorine substitution, on their organic ligands allows precise control over the electrical and mechanical properties of the materials [9, 22–24]. The introduction of strongly electronegative functional groups can significantly enhance the electron affinity of MOFs, facilitating charge transfer during contact electrification. Meanwhile, the well-defined nanostructures of MOFs increase the surface roughness of composite films, thereby enlarging the effective contact area and further improving the triboelectric output [25, 26]. In the field of SCs, MOFs show great potential as novel electrode materials due to their tunable conductivity and porous structure [27–29]. The UiO-66 series, in particular, provides a new strategy for enhancing the performance of dielectric layers of SCs, leveraging their unique functional frameworks and the open-channel structures [30, 31]. The introduction of strongly electronegative groups via organic ligands enhances the charge adsorption capacity on the material surface,

while the porous skeleton facilitates efficient ion transport pathways.

Based on our prior research, this study presents a multifunctional strategy using fluorinated MOF (UiO-66-4F) to develop a high-performance flexible system that integrates triboelectric energy harvesting and storage (Figure 1). UiO-66-4F was first introduced as a multifunctional filler into a PDMS matrix to systematically enhance TENG output, including voltage, current, power, and stability. It was then combined with lithium salt in PDMS to improve ion conductivity, capacitance, and frequency response in SCs. Finally, an optimized MOF-based TENG was integrated with an MOF-based SC through rational circuitry. The comprehensive performance of the assembled device was assessed, with a focus on its sustained energy supply, output stability, and ability to power small electronics. This work confirms the promise of fluorinated MOFs as dual-mode enhancers for flexible energy systems and offers a new material design pathway for high-performance, sustainable electronics.

2 Experimental

2.1 Materials

Tetrafluoroterephthalic acid (99%, Beijing HWRK Chem Co., Ltd., Beijing, China) and zirconium nitrate pentahydrate ($Zr(NO_3)_4{\cdot}5H_2O$, analytical grade) were used as the main precursors for the synthesis of UiO-66-4F. Acetic acid (CH_3COOH, analytical grade) and n-hexane (analytical grade) were obtained from Shanghai Macklin Biochemical Co., Ltd. (Shanghai, China) and Tianjin Fuyu Fine Chemical Co., Ltd. (Tianjin, China), respectively. Polydimethylsiloxane (PDMS, Sylgard 184) was purchased from Dow Chemical Co. (Shanghai, China). All reagents were of analytical grade and used as received without further purification. Ultrapure water (resistivity 18.2 MΩ cm) was produced using a SMART ultrapure water purification system (Heal Force, Shanghai, China) and employed in all aqueous solution preparations.

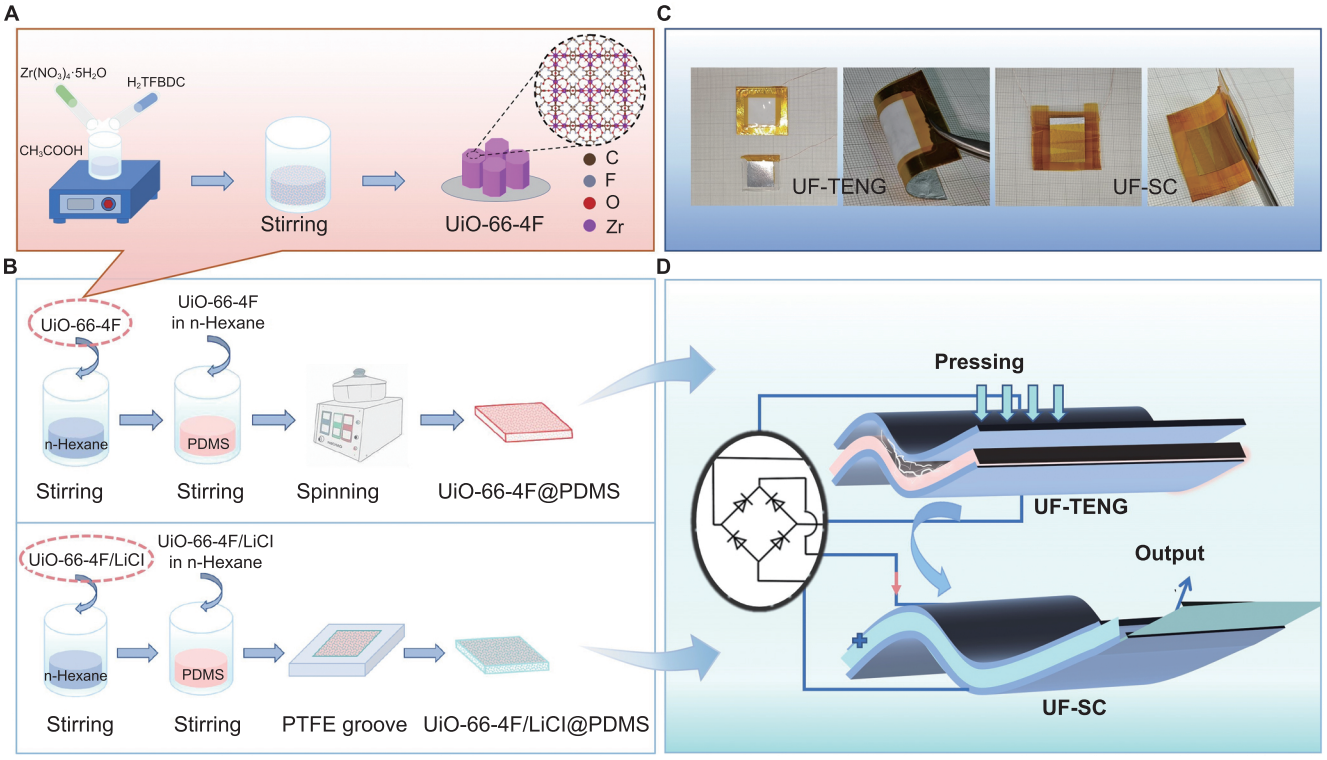

Figure 1 Synthesis, fabrication, and integration of UiO-66-4F-based self-powered systems. (A) Synthetic and preparation of UiO-66-4F. (B) Fabrication process of UiO-66-4F@PDMS and UiO-66-4F/LiCl@PDMS composite films. (C) Photographs of UF-TENG and UF-SC devices under flat and bent states. (D) Schematic illustration of the integrated UF-TENG -SC system for energy harvesting and storage

2.2 Characterization methods

Scanning electron microscopy (SEM, Apreo HiVac) was employed to characterize the surface and cross-sectional morphologies of UiO-66-4F and its composite films, revealing their microstructural features. The crystalline structures of the samples were characterized using an X-ray diffractometer (XRD, D8 ADVANCE), with measurements conducted under Cu Kα irradiation at a wavelength of 1.5406 Å. Fourier transform infrared spectroscopy (FTIR, Nicolet iS50) was also used for structural identification, with testing covering a spectral range of 400–4,000 cm^{-1}. The electrochemical performance of the UiO-66-4F/LiCl@PDMS composite membrane with a nanostructured architecture was evaluated using electrochemical impedance spectroscopy (EIS), galvanostatic charge-discharge (GCD) measurements, and cyclic voltammetry (CV) analysis. The short-circuit current, output voltage, and transferred charge of the flexible energy-harvesting device were recorded using an electrometer (Keithley 6517B) and a data acquisition card (NI USB-6356) at room temperature. The mechanical flexibility of the composite films was tested using a stepper motor system (KH-01). During the measurement, the samples were mounted onto the clamping fixture of the motor, and the stretching displacement was accurately controlled by the KH-01 controller.

2.3 Synthesis of UiO-66-4F

UiO-66-4F was synthesized via a room-temperature stirring method. Typically, 1.2 g (1.26 mM) of 2,3,5,6-tetrafluoroterephthalic acid (TFTPA) and 3.35 g (1.95 mM) of zirconium nitrate pentahydrate ($Zr(NO_3)_4{\cdot}5H_2O$) were separately dissolved in 40 mL of ultrapure water under ultrasonication until complete dissolution. The two solutions were then combined in a 200 mL beaker containing a magnetic stir bar, followed by the addition of 10 mL (43.7 mM) of glacial acetic acid as a modulator. The mixture was sealed and magnetically stirred at room temperature for 40 h, resulting in a white precipitate. The obtained solid was collected by centrifugation (8,000 rpm, 5 min), washed three times with ultrapure water and twice with anhydrous ethanol, and then air-dried at room temperature. Finally, the dried product was ground uniformly for 20 min to obtain fine UiO-66-4F powder for subsequent use.

2.4 Preparation of UiO-66-4F@PDMS and UiO-66-4F/LiCl@PDMS composite films

Pre-ground UiO-66-4F powder was dispersed in n-hexane and stirred for 1 h to form a uniform suspension. PDMS prepolymer and curing agent (10:1, w/w) were then added, and the mixture was stirred for another hour to ensure homogeneity. The composite precursor was spin-coated onto polyethylene terephthalate (PET) substrates (2,000 rpm, 10 s, three cycles) and cured at 80°C for 2 h. During curing, n-hexane evaporated completely, yielding flexible UiO-66-4F@PDMS films (~120 μm thick). Pure PDMS films were fabricated under identical conditions for comparison.

Pre-ground UiO-66-4F powder was mixed with anhydrous LiCl (50 wt%) and ground for 20 min to ensure uniform blending. The mixture was dried at 120°C for 1 h and then dispersed in 1 mL of n-hexane under sealed stirring for 1 h. PDMS prepolymer and curing agent (10:1, w/w) were added, and the resulting suspension was stirred for another hour. The composite precursor was cast into PTFE molds (3 cm × 3 cm, 0.3 mm thick) and cured at 80°C for 2 h. After complete solvent evaporation, flexible UiO-66-4F/LiCl@PDMS films (~120 μm thick) were obtained.

2.5 Fabrication of UF-TENG and UF-SC devices

The TENG was fabricated in a contact-separation mode. PET (3 cm × 3 cm) films served as flexible substrates, with sponge layers attached to both sides to provide cushioning during operation. Conductive aluminum tapes were used as flexible electrodes, and copper wires were fixed to their edges with Kapton tape for electrical connection. Pre-fabricated UiO-66-4F@PDMS films with various filler ratios were adhered to the lower electrodes to construct UiO-66-4F-based TENGs (UF-TENGs), in which Al and UiO-66-4F@PDMS acted as the triboelectric pair. For comparison, a PDMS-based TENG (PD-TENG) was prepared under identical conditions using pure PDMS films as the friction layer. Each device had an effective working area of 2 cm × 2 cm, and energy generation was achieved through periodic vertical contact-separation cycles.

The solid-state SC was assembled in a symmetric configuration. PET (3 cm × 3 cm) films were used as flexible substrates, with double-sided conductive aluminum tapes serving as electrodes. Copper wires were attached to the tape edges using Kapton tape for a stable electrical connection. The pre-fabricated UiO-66-4F/LiCl@PDMS composite film was laminated onto the lower electrode as the dielectric layer, followed by alignment and attachment of the upper electrode to form a UiO-66-4F/LiCl@PDMS-based supercapacitor (UF-SC). During assembly, firm contact between the dielectric and electrodes was maintained to eliminate air gaps and ensure consistent performance. The effective working area of each device was 2 cm × 2 cm, and a slight pressure was applied during encapsulation to enhance interfacial adhesion and device stability.

2.6 Assembly of UF-TENG-SC integrated devices

The UF-TENG-SC integrated device was assembled by connecting UF-TENG and UF-SC in series using copper wires. The integration circuit was realized through an external rectifier bridge, with both devices maintaining independent electrodes to enable efficient energy harvesting and storage. The rectifier bridge ensured unidirectional current transmission from the UF-TENG, thereby reducing energy loss and improving the overall energy utilization efficiency. Both components were fixed onto a flexible PET substrate (3 cm × 3 cm) and mechanically reinforced with Kapton tape to ensure stability and durability during operation.

3 Results and Discussion

3.1 Fluorinated MOF-enabled triboelectric harvester

A fluorinated UiO-66 derivative, denoted as UiO-66-4F, was successfully synthesized via a hydrothermal method by incorporating tetrafluorinated side-chain substituents. The morphology and structure of UiO-66-4F were systematically characterized using SEM, XRD, and FTIR spectroscopy. As shown in Figure 2A, the particles exhibit uniform distribution and well-defined morphology. UiO-66-4F exhibits an octahedral morphology with a nearly spherical profile [22]. The high magnification SEM image (Figure 2A inset) further clearly demonstrated the microstructure of the particle surface. The results of particle size analysis (Figure 2D) indicate that the average particle size is about 450–500 nm. Particle size analysis indicates that UiO-66-4F particles are in the sub-micron scale, exhibiting a narrow and approximately standard distribution. It indicates that the MOF material has controlled crystallization growth and good homogeneity of the particle size of crystal particles during the synthesis process. The XRD pattern of UiO-66-4F (Figure 2B) displays characteristic diffraction peaks at $2\theta = 7.32°$, 12.01°, 14.05°, 18.39°, 22.13°, and 25.42°, corresponding respectively to the (111), (022), (113), (004), (115), and (224) crystal planes of the UiO-66-type framework [32, 33]. These diffraction peaks align well with the typical diffraction features of UiO-66, confirming that the material retains the crystalline structure of this MOF family [22]. In the FTIR spectra (Figure 2C), the disappearance of the C=O stretching vibration peak at 1,694 cm^{-1} (originating from the H_2TFBDC ligand) indicates successful coordination of the ligand to the Zr node. Concurrently, a new absorption peak emerges at 1,610 cm^{-1}, attributed to the asymmetric stretching vibration of the Zr–O bond. Additional peaks are observed at 1,585 cm^{-1} (asymmetric stretching of O–C–O), 738 cm^{-1} (O–H vibration), and 660 cm^{-1} (C–H vibration), collectively corroborating the formation of a stable coordination architecture between the ligand and the metal cluster. Moreover, the presence of a distinct peak at 1,268 cm^{-1} confirms the incorporation of C–F bonds, verifying the successful introduction of fluorine-containing substituents into the framework. The vibration of C=O on the benzene ring and the stretching vibration of the C–O bond in –COOH were observed at 1,405 and 1,000 cm^{-1}, respectively, which further proved the structural integrity of the material and the retention of the ligand functional groups. The porosity of UiO-66-4F was evaluated by N_2 adsorption-desorption measurements (Figure 2E). The Brunauer-Emmett-Teller (BET) surface area was calculated to be 117.9 $m^2\ g^{-1}$. Pore-size distribution analysis derived from the Barrett-Joyner-Halenda (BJH) method (Figure 2F) shows a dominant pore-size range of 3–5 nm, confirming a hierarchical micro-mesoporous structure [34]. Such a porous architecture provides a

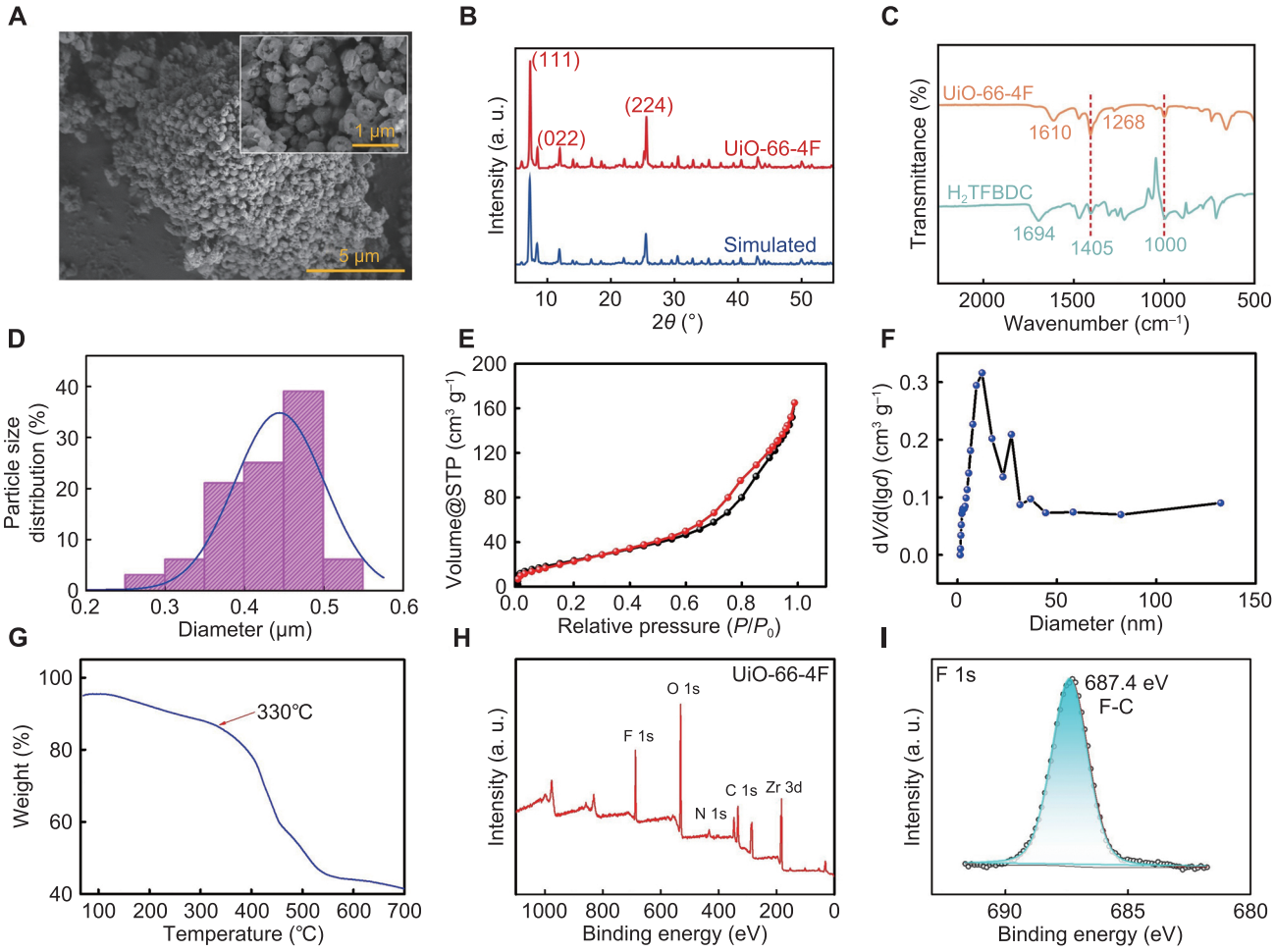

Figure 2 Morphology and structural characterization of UiO-66-4F. (A) SEM image of UiO-66-4F, with an inset showing a high-magnification view. (B) Experimental XRD pattern and simulated trace generated from crystallographic information file data. (C) FTIR spectra comparing UiO-66-4F with the 2,3,5,6-tetrafluoroterephthalic acid (H_2TFBDC) linker. (D) Particle size distribution. (E) Nitrogen (N_2) adsorption-desorption isotherms at 77 K. (F) Pore size distribution derived from the desorption branch using the BJH method. (G) TGA of UiO-66-4F. (H) XPS survey and (I) corresponding deconvoluted spectra of F 1s of the UiO-66-4F

high specific surface area and efficient ion transport pathways, which are beneficial for enhancing interfacial contact and electrochemical performance in composite films. The moderate amount of micron-sized, narrowly distributed UiO-66-4F particles can be uniformly dispersed and inhibit agglomeration in PDMS. They can easily form a moderate degree of roughness on the contact surface, thereby increasing the actual contact area and enhancing the local electric field.

Thermogravimetric analysis (TGA) was used to evaluate the thermal stability of UiO-66-4F. As shown in Figure 2G, the material mass decreased during the warming process, which mainly originated from the removal of water molecules adsorbed inside the material and residual organic solvents. It is worth noting that the skeleton structure remains stable below 330°C without significant collapse, indicating that UiO-66-4F possesses good thermal stability and can maintain its structural integrity within the operating temperature range of the device, which is conducive to guaranteeing the long-term operational stability of the device. In order to confirm the intrinsic chemical structure and surface elemental states of the synthesized UiO-66-4F material, we performed X-ray photoelectron spectroscopy (XPS) analysis. The full-spectrum scanning results (Figure 2H) confirm that the material is mainly composed of Zr, O, C, N, and F elements. Among them, the fluorine 1s high-resolution spectrum (Figure 2I) shows a main peak at 687.4 eV, which is attributed to the C-F covalent bond formed between fluorine atoms

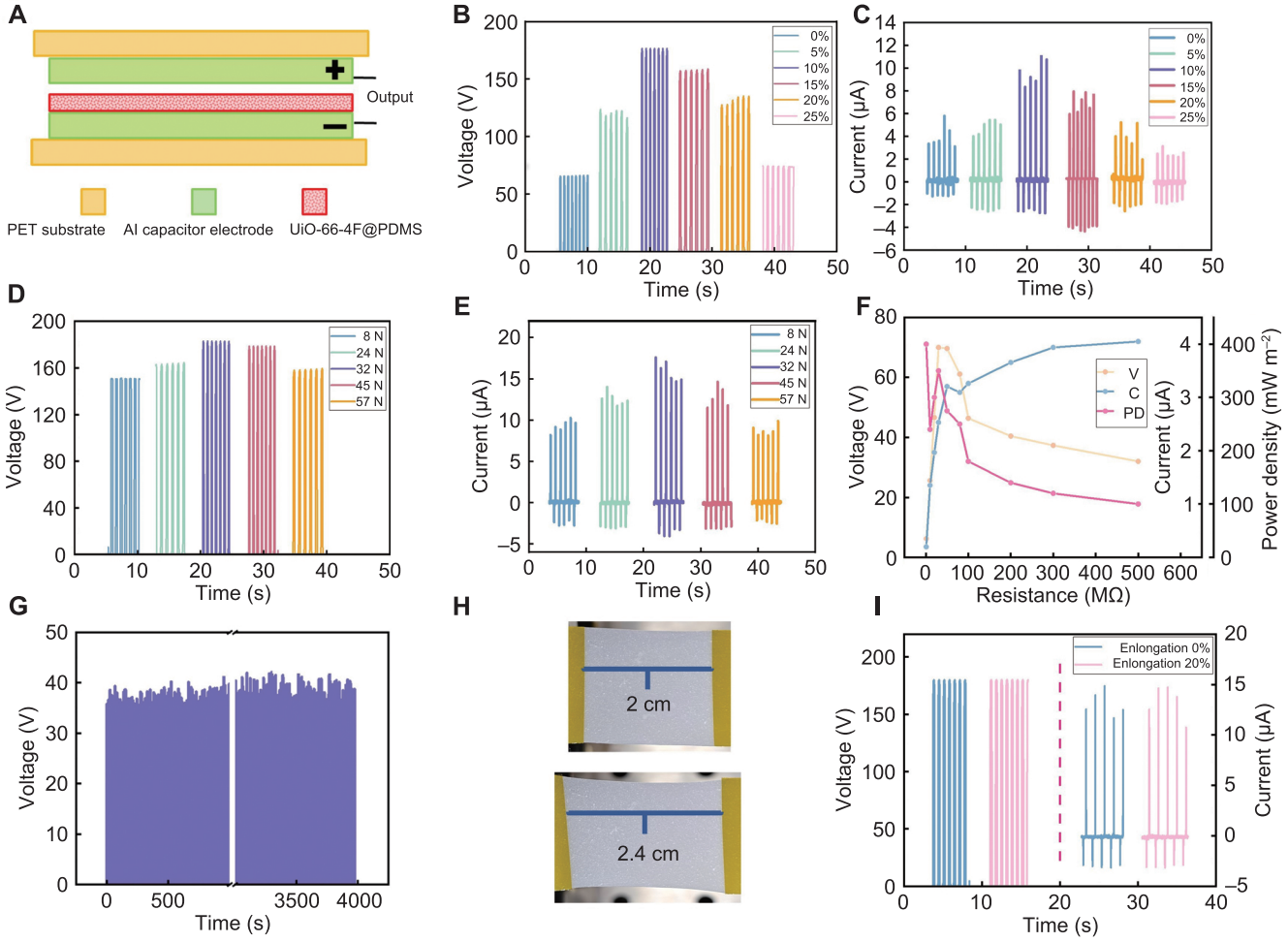

Figure 3 Structure and electrical performance of the UF-TENG. (A) Schematic of the UF-TENG device architecture. (B, C) Open circuit voltage and short circuit current of the UF-TENG with different fillers under a constant force and frequency. (D, E) Open circuit voltage and short circuit current of the 10 wt% UF-TENG under different applied forces. (F) Output voltage, current, and instantaneous power of the UF-TENG under various external load resistances, highlighting the maximum power point. (G) Stability of the open circuit voltage over >7,000 operating cycles under a 50 MΩ load. (H) Photographs of the 10 wt% UiO-66-4F@PDMS film in the undeformed state and at 20% tensile strain. (I) Comparison of open circuit voltage and short circuit current for the 10 wt% UF-TENG before stretching and after 10,000 cycles at 20% tensile strain

and carbon atoms in UiO-66-4F. The symmetry of the peak shape and the absence of signals of fluorine species at other binding energy positions indicate that the chemical environment of fluorine in the material is homogeneous.

The preparation of homogeneous composite films is crucial for optimizing device performance. To achieve this, a pre-dispersion strategy was employed, in which milled UiO-66-4F was first dispersed in n-hexane to form a stable suspension. This suspension was then thoroughly mixed with the PDMS elastomer and subsequently cured to obtain uniformly doped UiO-66-4F@PDMS composite films. As illustrated in Figure 3A, the resulting UiO-66-4F@PDMS-based triboelectric nanogenerator (UF-TENG) adopts a vertical contact-separation structure, with an aluminum (Al) electrode and the UiO-66-4F@PDMS composite film serving as the two contact layers. Surface and cross-sectional SEM images of the pure PDMS film and the 10 wt% UiO-66-4F@PDMS composite film are presented in Figure S1. Compared with the pure PDMS film, the composite with 10 wt% UiO-66-4F concentration exhibits a distinct particulate microstructure, significantly enhanced surface roughness, and uniform particle distribution without noticeable agglomeration. These results confirm that the pretreatment dispersion step

effectively improves the dispersion of MOF particles within the polymer matrix.

The working principle of the TENG can be described by the coupling of contact electrification and electrostatic induction (Figure S2) [35]. Upon the application of external pressure, the two contact layers come into contact. Owing to the significant difference in electron affinity between the Al electrode and the UiO-66-4F@PDMS composite film, electron transfer occurs at the interface, resulting in positive charges on the Al surface and negative charges on the composite film surface [16]. At this point, the system reaches an electrostatic equilibrium, and no current flows in the external circuit. When the external force is released, the layers separate while retaining their surface charges. This preserved charge separation creates a potential difference that induces charges of opposite polarity on the respective electrodes via electrostatic induction. This process drives electron flow in the external circuit, generating a unidirectional current pulse. As the separation distance increases, the induced potential and current decrease to zero, and the system attains a new equilibrium. Subsequent re-application of force brings the layers back into proximity, reversing the potential difference and causing electrons to flow in the opposite direction, thus producing a current pulse of reversed polarity. By repeating this cycle of contact and separation, the device continuously generates an alternating current output. The operating principle of the PD-TENG is similar to that of the UF-TENG, as both rely on periodic contact-separation to produce alternating current signals [8].

As shown in Figure 3, the influence of UiO-66-4F on the output performance of UF-TENG was systematically investigated. The open-circuit voltage (V_{oc}) and short-circuit current (I_{sc}) outputs of the devices with different doping ratios (0 wt%, 5 wt%, 10 wt%, 15 wt%, 20 wt%, and 25 wt%) were measured under a constant applied force (45 N) and frequency (1.2 Hz), as presented in Figure 3B, C. The results indicate that the output performance improved markedly with increasing UiO-66-4F content, reaching an optimum at 10 wt% doping. At this ratio, the device achieved a maximum V_{oc} of 180 V and an I_{sc} of 11 μA, demonstrating that a moderate amount of UiO-66-4F can effectively enhance TENG performance. However, further increasing the doping ratio to 15 wt% and above led to a noticeable decline in both voltage and current outputs. This decrease may be attributed to particle agglomeration at higher loadings or the formation of an excessively thick dielectric layer, either of which could hinder efficient interfacial charge transfer. In summary, a UiO-66-4F doping ratio of 10 wt% is optimal for achieving the highest triboelectric output in this system. The V_{oc} and I_{sc} of devices with this doping ratio were further evaluated under a constant frequency of 1.2 Hz while varying the applied force (Figure 3D, E). As the applied force was increased from 8 to 32 N, the V_{oc} of the devices increased from about 145 V to a maximum value of 180 V, while the I_{sc} also increased from about 9 to 17 μA. This trend suggests that proper pressure can promote contact between the triboelectric layers and thereby improve charge-transfer efficiency [11]. However, when the force was further raised to 57 N, both outputs declined, the V_{oc} dropped to 155 V, and the I_{sc} decreased to around 10 μA. This reduction is likely caused by excessive compression of the triboelectric interface, which diminishes the effective contact area and hinders charge accumulation. Hence, external force modulation plays a critical role in determining the output performance of the TENG. Among the tested conditions, a force of about 32 N was identified as optimal, delivering the highest power-generation efficiency.

To further assess the performance of UF-TENG devices in practical scenarios, their output power and operational stability were systematically characterized. The devices were subjected to a constant mechanical force (45 N) and operating frequency (1.2 Hz) while varying the load resistance. The instantaneous output power was measured across different load resistances, exhibiting a trend of initial increase followed by a decrease as the resistance increased (Figure 3F). The maximum power density of approximately 400 mW m^{-2} was observed at a load resistance of 50 MΩ. Furthermore, the operational stability of the UF-TENG device with a doping ratio of 10 wt% was evaluated over an extended duration of 4,000 seconds under this matched resistance (Figure 3G), and the results showed that the output voltage remained highly stable throughout

the entire 4,000-second test period, with no apparent signs of degradation. The evaluated UF-TENG devices demonstrated outstanding output stability and reliable long-term performance. Furthermore, under a load test, the 10 wt% doped device proved capable of powering 44 interconnected LED beads continuously (45 N, 1.2 Hz), sufficient to illuminate them all, highlighting its potential for practical applications (Figure S3). The observed flickering of the LED beads arose from the operational principle of the UF-TENG, which inherently operates in a vertical contact-separation mode, resulting in an alternating current (AC) output.

The tensile durability of the composite films with a 10 wt% doping ratio was evaluated using a linear motor system controlled by Lin Mot-Talk software. After 10,000 cyclic tensile tests at 20% elongation, the UiO-66-4F@PDMS composite films largely retained their original integrity, with well-preserved surface morphology and no noticeable cracks, confirming their excellent flexibility (Figure 3H). To further investigate the influence of mechanical cycling on electrical output, the V_{oc} and I_{sc} of the corresponding TENG device were measured under a 45 N force and 1.2 Hz operating frequency, both before and after the stretching process (Figure 3I). The results confirmed that the electrical output of the devices was not compromised by the mechanical stretching, with well-maintained performance after 10,000 cycles at 20% elongation. It indicates that the UiO-66-4F@PDMS composite film offers both superior flexibility and contributes to the outstanding output stability of the resulting TENGs, thereby validating the potential of UF-TENG for use in flexible wearable self-powered systems.

3.2 Fluorinated MOF-assisted storage unit

Flexible solid-state supercapacitors based on polymer dielectrics, such as PDMS, often suffer from low ionic conductivity and limited interfacial charge storage, which limit their achievable energy and power densities. To address these challenges, we developed a flexible dielectric composite film, denoted as UiO-66-4F/LiCl@PDMS, by embedding UiO-66-4F and LiCl into a PDMS matrix. The addition of LiCl serves as a lithium-ion source, whose dissociated Li^+ ions can transport through the porous framework of UiO-66-4F, thereby substantially enhancing the ionic conductivity of the composite solid electrolyte [36, 37]. A pre-dispersion strategy combined with a scraping coating technique was employed to achieve a homogeneous distribution of the MOF particles and LiCl within the polymer. The surface morphology of the 20 wt% UiO-66-4F/LiCl@PDMS composite film (Figure S4) showed an apparent increase in roughness and a relatively uniform particle distribution, without significant agglomeration, demonstrating excellent doping uniformity and a homogeneous internal structure. Given these favorable structural characteristics, a flexible supercapacitor (UF-SC) was constructed based on this composite film. We systematically evaluated the device performance by studying the influence of key parameters, including doping ratio, voltage window, and scan rate, through CV and EIS.

The fabricated device had an effective working area of 2 cm × 2 cm and was lightly pressed to enhance interfacial adhesion. As shown in Figure 4A, UF-SC was constructed with a symmetric architecture, in which the UiO-66-4F/LiCl@PDMS composite film served as the dielectric layer, sandwiched between two flexible electrodes composed of double-sided conductive aluminum tapes. EIS was performed on UF-SC devices incorporating composite films with varying doping ratios (5%–25%) over a frequency range of 0.1 Hz to 100 kHz at a voltage amplitude of 50 mV. The Nyquist plots (Figure 4B) exhibited no semicircular arc in the high-frequency region at any doping ratio, indicating low interfacial charge-transfer resistance and behavior consistent with typical double-layer capacitors [33]. As the doping ratio increased, the device impedance initially decreased and then increased, reaching minima of approximately 300 and 320 Ω at 15 wt% and 20 wt% doping ratios, respectively. In the corresponding Bode plot (Figure 4C), the phase angles approach −90° at low frequencies and remain stable up to 100 kHz, indicating nearly ideal capacitive characteristics. Based on these results, the UF-SC device with a 20 wt% doping ratio was selected for further experiments due to its optimal impedance and close-to-ideal capacitive behavior. Although the 15 wt% device showed the lowest absolute impedance, the 20 wt% device was selected for further experiments due to its optimal combination

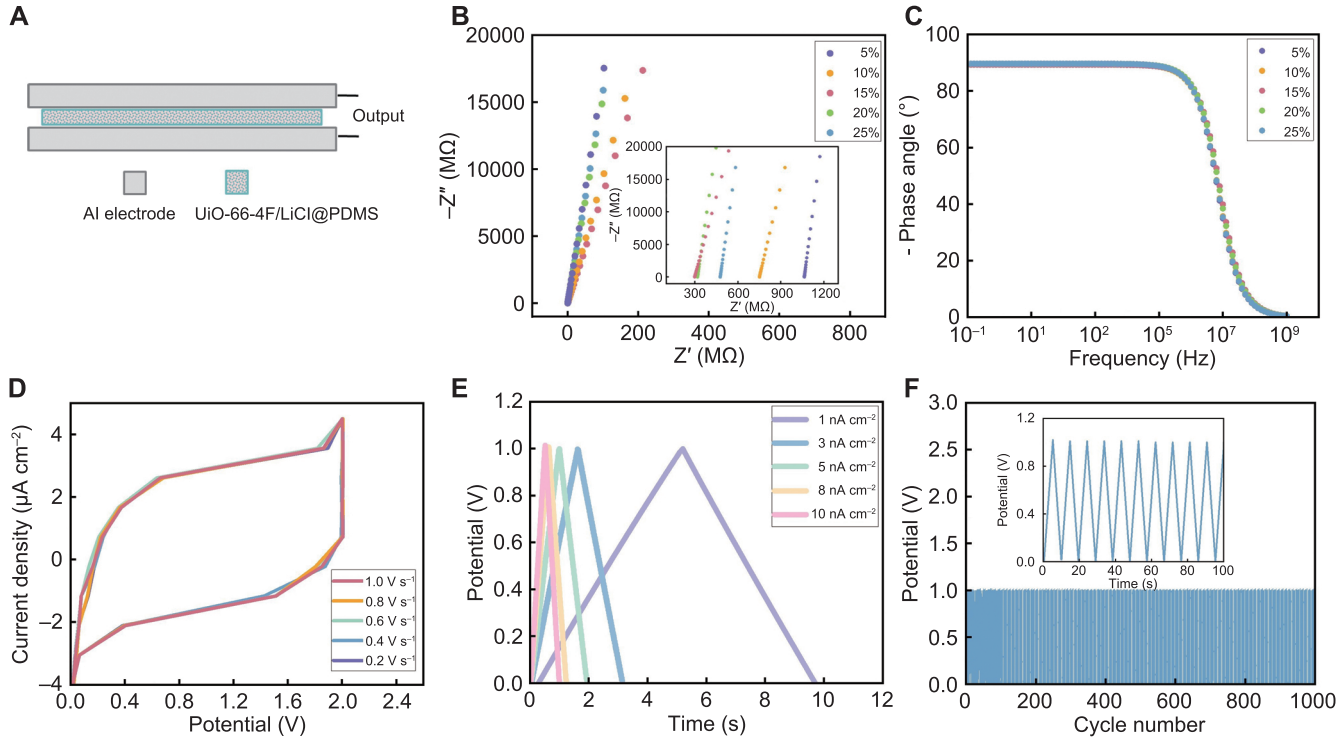

Figure 4 Structure and electrochemical characterization of the UF-SC. (A) Schematic of the UF-SC device architecture. (B) Nyquist plots of UF-SC with different filler loadings (AC perturbation amplitude: 50 mV). (C) Bode plots. (D) Cyclic voltammograms of the 20 wt% UF-SC at various scan rates within a 2 V window. (E) GCD curves at different current densities. (F) Cycling stability under a constant current of 1 nA for 1,000 cycles, the inset displays the voltage-time trace for cycles 900–910

of low impedance and the closest-to-ideal capacitive behavior (phase angle nearest to −90°), suggesting a better balance between ion transport and charge storage. EIS was also performed on the selected 20 wt% UF-SC device under varying voltage amplitudes (10–100 mV). As shown in Figure S5a, the Nyquist plots nearly overlapped across all amplitudes, with impedance values stable between 300 and 360 Ω. The corresponding Bode plots further revealed minimal fluctuation in phase angle (Figure S5b), which consistently approached -90° at low frequencies and remained stable up to 100 kHz. These results indicate that the ion migration pathways in the composite film remain effectively open under different electric fields. It not only facilitates rapid ion transport to the electrode interface but also enables the efficient formation and release of the electric double layer throughout the operating voltage range.

The CV tests were performed on the 20 wt% UF-SC at different voltage windows (1.0–2.0 V) with a scan rate of 0.1 V s^{-1} (Figure S6). As depicted, its CV curve shows a pair of weak redox peaks under the 2 V voltage window. The electrochemical reaction is mainly controlled by the diffusion kinetics of electrolyte ions. The redox peak can be attributed to the reversible Faraday reaction occurring in the LiCl electrolyte in the composite film and contributed by the Cl^- redox pair. The CV curves exhibit good symmetry across all windows, reflecting high electrochemical reversibility [38]. Although the integrated CV area increased with expanding voltage window, slight polarization was observed at 2.0 V. This voltage was therefore selected for subsequent CV scans at various rates (0.2–1.0 V s^{-1}). As shown in Figure 4D, the CV curves retained highly symmetric and rectangular shapes even at elevated scan rates, indicating excellent ion diffusion kinetics and capacitance retention [39]. The GCD curve data in Figure 4E demonstrate that within the entire potential window set in the experiment, the capacitance exhibits a linear variation trend with the current density, and no obvious ohmic drop occurs. This characteristic not only fully verifies its excellent capacitive performance but also reflects its favorable conductivity, along with

excellent reversibility and rapid *I-V* response capability (Figure 4F). These outstanding electrochemical properties can be attributed to the UiO-66-4F skeleton, which offers the composite film abundant interconnected ion channels [40]. These channels enable LiCl ions to migrate rapidly to the electrode surface and form a stable bilayer, and this bilayer not only effectively suppresses diffusion polarization but also improves the device's energy storage efficiency during rapid charge-discharge cycles [41].

3.3 Fluorinated MOF enable harvesting and storage integration

The UF-TENG based on UiO-66-4F@PDMS composite film demonstrates a high efficiency in converting mechanical energy into electricity. The UF-SC constructed from the UiO-66-4F/LiCl@PDMS composite film exhibits low impedance and high ionic conductivity. In this work, an integrated UF-TENG-SC device was fabricated by connecting UF-TENG and UF-SC via a rectifier bridge in an external circuit to investigate the interaction between the two and the performance of the integrated device. The schematic diagram of the structure and the physical photograph of the UF-TENG-SC integrated device are shown in Figure 5A and Figure 5B, respectively. The device adopts a free-standing integrated architecture that leverages the high output of the UF-TENG and the favorable capacitive behavior of the UF-SC. In the integrated system, the UF-TENG operates in contact-detachment mode. Upon contact, electron transfer occurs between the Al electrode and the UiO-66-4F@PDMS composite film due to their different electron affinities, leaving the Al electrode positively charged and the composite film

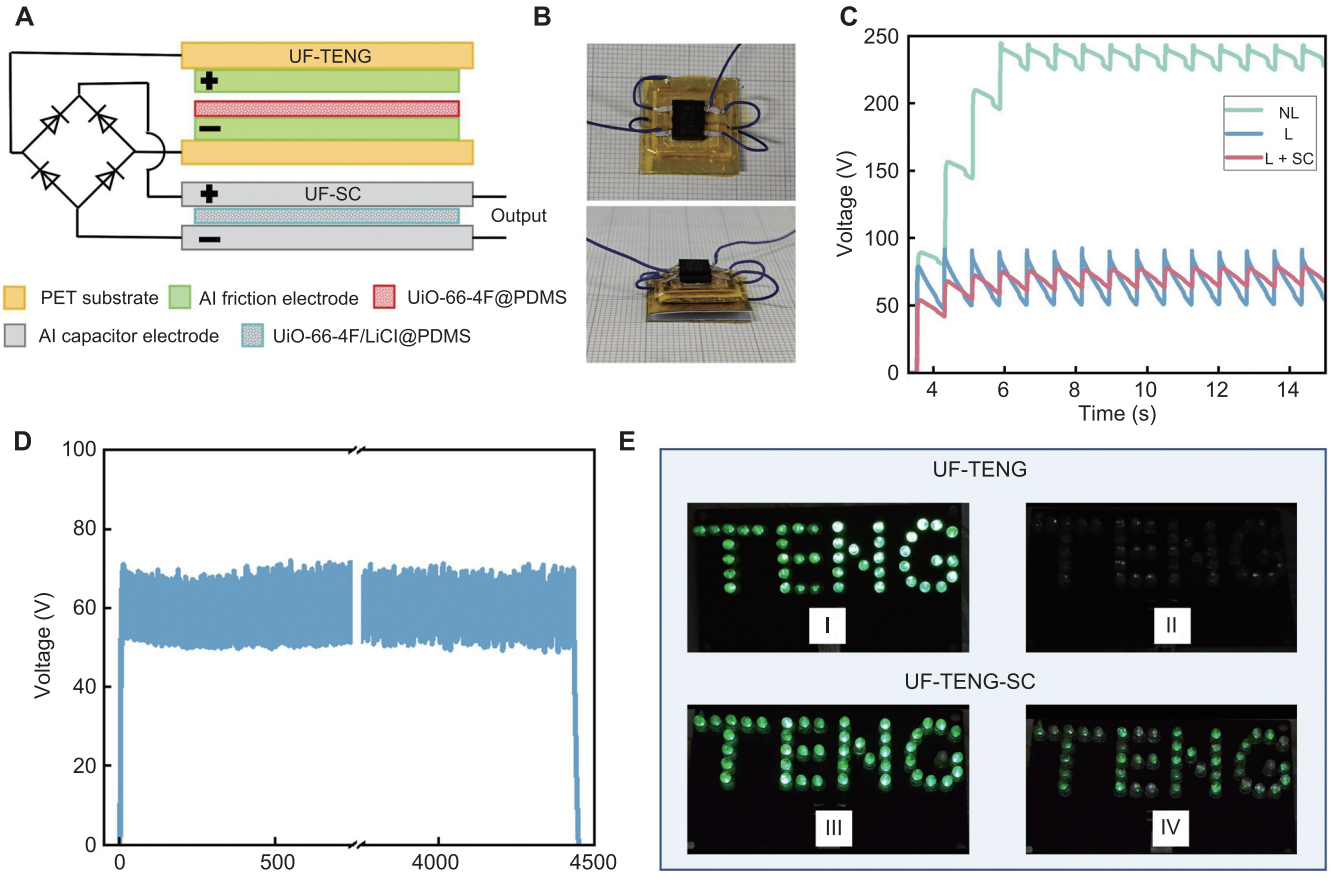

Figure 5 Architecture, demonstration, and output stability of the UF-TENG-SC integrated device. (A) Schematic of the UF-TENG-SC integrated architecture. (B) Photograph of the assembled integrated device. (C) Output voltage of the UF-TENG under different load resistances. (D) Output-stability test of the UF-TENG-SC integrated device under a representative load. (E) Optical images of LED illumination, (I) maximum and (II) minimum brightness driven by the standalone UF-TENG, (III) maximum and (IV) minimum brightness when powered by the UF-TENG-SC integrated device

negatively charged. During separation, electrostatic induction drives electron flow in the external circuit, generating an alternating current that is rectified and directed to the UF-SC. The UF-SC operates via an electric double-layer mechanism, with the UiO-66-4F/LiCl@PDMS composite serving as the dielectric layer. Under an applied electric field, Li^+ and Cl^- ions dissociated from LiCl migrate through the ion channels provided by UiO-66-4F [41]. During charging, Li^+ moves toward the negative interface and Cl^- toward the positive interface, forming an electrical double layer that stores charge [42, 43]. The pulsed electrical energy output from the UF-TENG goes through rectification for charging the UF-SC. The UF-SC suppresses voltage fluctuations of the UF-TENG by storing and releasing ionic charge, making the integrated device output more stable and enabling the conversion of mechanical energy to stable electrical energy via ionic charge storage. The uniform dispersion of all components within the composite films is critical for device performance. As directly evidenced by energy-dispersive X-ray spectrometry (EDS) mapping (Figure S7), the Zr (from UiO-66-4F) and Si (from PDMS) signals are evenly distributed in the UiO-66-4F@PDMS film, while the UiO-66-4F/LiCl@PDMS film exhibits a homogeneous distribution of Zr, Si, and Cl (from LiCl) signals. This result conclusively confirms the desired compositional homogeneity across the films.

The output voltage of the UF-TENG unit with the UF-TENG-SC integrated device was evaluated under an applied force of 45 N and a frequency of 1.2 Hz (Figure 5C). Under open-circuit conditions (green curve), the UF-TENG generated a high output voltage, yet the energy could not be efficiently utilized without an external load. When directly connected to LED loads (blue curve), the output voltage dropped markedly and exhibited periodic fluctuations. These reductions and fluctuations arise because the LEDs consume part of the generated power, and the inherent pulsed output characteristic of the TENG further contributes to voltage instability. In contrast, when the integrated UF-TENG-SC device was connected to the same LED loads (red curve), the voltage fluctuation was substantially suppressed, yielding a more stable overall output. This result demonstrates that incorporating the UF-SC effectively enhances the voltage stability and optimizes the output performance of the UF-TENG under loaded conditions. As shown in Figure 5E, when the UF-TENG drives LEDs directly, the LED beads flicker noticeably due to large voltage fluctuations. By contrast, the integrated UF-TENG-SC device powers the same LEDs with markedly suppressed voltage fluctuations and significantly improved stability. Although the brightness of the loaded LED beads is on the low side, they can be maintained in a constant state. In addition, stability analysis of the UF-TENG-SC integrated device over 4,500 s (Figure 5D) confirms that its output voltage remains essentially stable. This stable output performance of the UF-TENG-SC integrated device shows its potential for applications in self-powered systems for flexible wearable electronic devices. The integrated UF-TENG-SC system effectively converts human mechanical energy into stable electrical energy via the UF-TENG, while through the UF-SC, ensuring steady operation of functional modules and reliable signal transmission.

4 Conclusions

To address the problems of single-functionality and insufficient stability of friction-layer materials for TENGs, and the low ionic conduction efficiency of SCs, metal-organic framework materials (UiO-66-4F) with strong electronegativity were designed and synthesized in this study. UiO-66-4F was composited with polydimethylsiloxane (PDMS), and UiO-66-4F@PDMS and UiO-66-4F/LiCl@PDMS composite films were prepared. High-performance UF-TENG-SC integrated devices consisting of UF-TENG and UF-SC units were constructed based on them. The UF-TENG containing 10 wt% UiO-66-4F achieved an open-circuit voltage up to 180 V and a short-circuit current up to 11 μA, which are four and six times higher than those of PD-TENG, respectively. The high specific surface area of UiO-66-4F increases the effective contact area of the friction layer, while its strong electronegativity promotes directional charge transfer. The UF-SC with 20 wt% UiO-66-4F exhibits a low impedance of 320 Ω at high frequency and a low-frequency phase angle close to −90°, demonstrating typical double-layer capacitance characteristics. The abundant porous structure of

UiO-66-4F provides efficient ion migration channels for Li^+ and Cl^- dissociated from LiCl, thereby accelerating ion transfer and enhancing the supercapacitor's Performance. By integrating the UF-TENG and the UF-SC via a rectifier bridge, a freestanding, integrated energy-harvesting-storage device was constructed. This integrated UF-TENG-SC device exhibits excellent voltage regulation and stable output capability. Within self-powered flexible wearable electronics, such an integrated approach shows promising application potential. It can efficiently convert the mechanical energy generated by human movement into electrical energy while utilizing the UF-SC to stabilize the output, thereby supplying power to sensors and other functional modules. Ultimately, the system achieves monolithic integration of energy harvesting, storage, and regulated power delivery.

Author Contributions

Jing Liu: Investigation; data curation; formal analysis; writing - original draft; writing - review & editing. Dong Wang: Data curation; formal analysis; investigation; software. Dingyi Yang: Data curation; investigation; methodology; validation. Yong Wang: Formal analysis; resources; software; visualization. Yizhang Wu: Resources; formal analysis; writing - review & editing. Yong-Mei Wang: Conceptualization; formal analysis; funding acquisition; project administration; writing - review & editing.

Acknowledgements

This work was supported by the National Natural Science Foundation of China (Grant No. 52202186), S&T Program of Energy Shaanxi Laboratory (Grant No. ESLB202421), Xidian University Specially Funded Project for Interdisciplinary Exploration (Grant No. TZJH2024053).

Conflict of Interests Statement

The authors declare that they have no conflict of interest.

Data Availability Statement

The data that support the findings of this study are available from the corresponding author upon reasonable request.

References

1. W. Zhang, X. Wang, J. Duan, et al., "Recent Research Advances in Textile-Based Flexible Power Supplies and Displays for Smart Wearable Applications," *ACS Appl. Electron. Mater.* 6, no. 8 (2024): 5429–5455, https://doi.org/10.1021/acsaelm.4c00606.
2. Z. Li, Y. Shen, C. Fang, Y. Huang, X. Yu, and L. Jiang, "Thermo-Electrochemical Cells Enable Efficient and Flexible Power Supplies: From Materials to Applications," *Energy Storage Mater.* 74 (2025): 103902, https://doi.org/10.1016/j.ensm.2024.103902.
3. X. Fan, B. Liu, J. Ding, et al., "Flexible and Wearable Power Sources for Next-Generation Wearable Electronics," *Batteries Supercaps* 3, no. 12 (2020): 1262–1274, https://doi.org/10.1002/batt.202000115.
4. Z. Lai, J. Xu, C. R. Bowen, and S. Zhou, "Self-Powered and Self-Sensing Devices Based on Human Motion," *Joule* 6, no. 7 (2022): 1501–1565, https://doi.org/10.1016/j.joule.2022.06.013.
5. Y. Han, Y. Liu, Y. Zhang, et al., "Functionalized Quasi-Solid-State Electrolytes in Aqueous Zn-Ion Batteries for Flexible Devices: Challenges and Strategies," *Adv. Mater.* 37, no. 1 (2025): 2412447, https://doi.org/10.1002/adma.202412447.
6. D. Han, Y. Wang, W. Lv, et al., "Micro Lithium Batteries toward the Next-Generation Smart Microsystems: A Review," *Energy Storage Mater.* 81 (2025): 104522, https://doi.org/10.1016/j.ensm.2025.104522.
7. Z. Ren, L. Wu, Y. Pang, W. Zhang, and R. Yang, "Strategies for Effectively Harvesting Wind Energy Based on Triboelectric Nanogenerators," *Nano Energy* 100 (2022): 107522, https://doi.org/10.1016/j.nanoen.2022.107522.
8. M. Shanbedi, H. Ardebili, and A. Karim, "Polymer-Based Triboelectric Nanogenerators: Materials, Characterization, and Applications," *Prog. Polym. Sci.* 144 (2023): 101723, https://doi.org/10.1016/j.progpolymsci.2023.101723.
9. D. Yang, Y. Xu, Y. Liu, et al., "Layer- and Temperature-Dependent Work Function Modulation in Crsbr," *CHAIN* 2, no. 3 (2025): 256–266, https://doi.org/10.23919/CHAIN.2025.000013.
10. M. Wang, D. Yang, Y. Wang, et al., "Multiferroic Coupling in Bilayer Janus 3r-Crscl," *Appl. Phys. Lett.* 127, no. 7 (2025): 072901, https://doi.org/10.1063/5.0288383.
11. G. Ramadasu, I. Woo, J. U. Yoon, S. J. Oh, P. Gajula, and J. W. Bae, "Boosting Triboelectric Performance of Pdms with Dual-Filler Reinforcement for Smart Touch Sensing," *J. Energy Chem.* 110 (2025): 455–465, https://doi.

org/10.1016/j.jechem.2025.07.001.

12. H. Zhang, D. Z. Zhang, D. Y. Wang, Z. Y. Xu, Y. Yang, and B. Zhang, "Flexible Single-Electrode Triboelectric Nanogenerator with Mwcnt/Pdms Composite Film for Environmental Energy Harvesting and Human Motion Monitoring," *Rare Met.* 41, no. 9 (2022): 3117–3128, https://doi.org/10.1007/s12598-022-02031-z.
13. H. Kim, N. Qaiser, and B. Hwang, "Electro-Mechanical Response of Stretchable Pdms Composites with a Hybrid Filler System," *Facta Universitatis, Series: Mechanical Engineering* 21, no. 1 (2023): 051–061, https://doi.org/10.22190/fume221205002k.
14. W. Akram, Q. Chen, G. B. Xia, and J. Fang, "A Review of Single Electrode Triboelectric Nanogenerators," *Nano Energy* 106 (2023): 108043, https://doi.org/10.1016/j.nanoen.2022.108043.
15. J. Liu, Y. Y. Cheng, H. Y. Wang, et al., "Regulation of Tio_2@ Pvdf Piezoelectric Nanofiber Membranes on Osteogenic Differentiation of Mesenchymal Stem Cells," *Nano Energy* 115 (2023): 108742, https://doi.org/10.1016/j.nanoen.2023.108742.
16. C. Yang, C. Ko, S. Chang, and M. Huang, "Study on Fabric-Based Triboelectric Nanogenerator Using Graphene Oxide/Porous Pdms as a Compound Friction Layer," *Nano Energy* 92 (2022): 106791, https://doi.org/10.1016/j.nanoen.2021.106791.
17. Y. T. Guo, S. C. Wu, S. H. Liu, et al., "Enhanced Dielectric Tunability and Energy Storage Density of Sandwich-Structured $Ba_{0.6}sr_{0.4}tio_3$/Pvdf Composites," *Mater. Lett.* 306 (2022): 130910, https://doi.org/10.1016/j.matlet.2021.130910.
18. S.P. Balmuchu and P. Dobbidi, "Temperature-Dependent Broadband Dielectric and Ferroelectric Properties of $Ba_{(1-X)}Sr_xtio_3$ Ceramics for Energy Storage Capacitor Applications," *J. Mater. Sci.: Mater. Electron.* 32, no. 7 (2021): 9623–9639, https://doi.org/10.1007/s10854-021-05624-z.
19. X. Meng, D. Hui, S. Ge, et al., "Nanopillar and Nanocone Structured $Srtio_3$/Pdms Films for Triboelectric Nanogenerators," *ACS Appl. Nano Mater.* 7, no. 12 (2024): 14193–14202, https://doi.org/10.1021/acsanm.4c01713.
20. P. K. Nitha and A. Chandrasekhar, "Marriage between Metal-Organic Frameworks/Covalent-Organic Frameworks and Triboelectric Nanogenerator for Energy Harvesting—a Review," *Mater. Today Energy* 37 (2023): 101393, https://doi.org/10.1016/j.mtener.2023.101393.
21. C. S. Patil, Q. M. Saqib, J. Kim, et al., "Synergistic Integration of Graphene Quantum Dots into Metal–Organic Framework-5 for Enhancing Triboelectric Nanogenerator Performance," *Adv. Compos. Hybrid Mater.* 7, no. 5 (2024), https://doi.org/10.1007/s42114-024-00980-w.
22. Y. M. Wang, X. X. Zhang, C. S. Liu, et al., "Remarkable Improvement of Mof-Based Triboelectric Nanogenerators with Strong Electron-Withdrawing Groups," *Nano Energy* 107 (2023): 108149, https://doi.org/10.1016/j.nanoen.2022.108149.
23. D. Sarkar, N. K. Das, K. K. Rao, and S. Badhulika, "Uio-66 (Zr)-F4 Mof Reinforced Anti-Freezing and Stretchable Piezoelectric Hydrogel-Based Triboelectric Nanogenerator for Self-Powered Epidermal Electronics in Sub-Zero Temperatures and Real-Time Ice-Cracking Alarm System," *Chem. Eng. J.* 521 (2025): 166528, https://doi.org/10.1016/j.cej.2025.166528.
24. Y. Q. Yang, L. Yang, Y. C. Zhao, H. Q. Pei, Z. X. Wen, and Y. C. Zhou, "Study on the Salt-Corrosion and Oxidation Role Mechanism of Ni-Based Single Crystal Superalloy in the Long-Term Hot Corrosion Environment," *J. Mater. Res. Technol.* 37 (2025): 25–40, https://doi.org/10.1016/j.jmrt.2025.05.233.
25. Y. Xu, D. Yang, Y. Zhang, et al., "Realizing Room-Temperature Ferromagnetism in Metal-Free Graphene through Vacancy-Assisted Hydrogenation," *CHAIN* 2, no. 1 (2025): 72–80, https://doi.org/10.23919/CHAIN.2025.000001.
26. Y. Wang, D. Yang, Z. Cheng, et al., "Strong Room-Temperature Ferromagnetism and Magnetocaloric Effect in Anisotropic Two-Dimensional Layered Chromium Indium Telluride," *Materials Futures* 4, no. 3 (2025), https://doi.org/10.1088/2752-5724/ade60f.
27. L. Pang, Y. Lei, Y. Zou, et al., "Revealing the Effects of Functional Group in Organic Linkers on Properties of Metal Organic Frameworks Electrode and Their Performance in Supercapacitors," *Chem. Eng. J.* 500 (2024): 157470, https://doi.org/10.1016/j.cej.2024.157470.
28. S. J. Shin, J. W. Gittins, C. J. Balhatchet, A. Walsh, and A. C. Forse, "Metal–Organic Framework Supercapacitors: Challenges and Opportunities," *Adv. Funct. Mater.* 34, no. 43 (2023): 202308497, https://doi.org/10.1002/adfm.202308497.
29. Y. Wang, D. Yang, S. Wang, et al., "P-Type Vdw Semiconductor Crscl Featuring Multipolarity Coexistence," *ACS Mater. Lett.* 7, no. 2 (2025): 636–645, https://doi.org/10.1021/acsmaterialslett.4c02378.
30. Y. Wang, T. Pan, G. Yuan, Q. Li, and H. Pang, "Mof and Mof-Derived Composites for Flexible Energy Storage Devices," *Compos. Commun.* 52 (2024): 102144, https://doi.org/10.1016/j.coco.2024.102144.
31. M. Li, Y. Zhang, H. Wang, et al., "Performance Enhancement of Self-Charging System by Combining Triboelectric Nanogenerators and Dielectric Capacitors," *Nano Energy* 119 (2024): 109073, https://doi.org/10.1016/j.nanoen.2023.109073.

32. W. Wen, Q. Zeng, P. Chen, et al., "Enhancing Li-Ion Conduction and Mechanical Properties Via Addition of Fluorine-Containing Metal—Organic Frameworks in All-Solid-State Cross-Linked Hyperbranched Polymer Electrolytes," *Nano Res.* 15, no. 10 (2022): 8946–8954, https://doi.org/10.1007/s12274-022-4523-z.
33. S. Zhao, M. Liu, Y. Zhang, et al., "Harvesting Mechanical Energy for Hydrogen Generation by Piezoelectric Metal-Organic Frameworks," *Mater Horiz* 9, no. 7 (2022): 1978–1983, https://doi.org/10.1039/d1mh01973b.
34. Z. Hu, Y. Peng, Z. Kang, Y. Qian, and D. Zhao, "A Modulated Hydrothermal (Mht) Approach for the Facile Synthesis of Uio-66-Type Mofs," *Inorg. Chem.* 54, no. 10 (2015): 4862–4868, https://doi.org/10.1021/acs.inorgchem.5b00435.
35. G. Zhu, C. Pan, W. Guo, et al., "Triboelectric-Generator-Driven Pulse Electrodeposition for Micropatterning," *Nano Lett.* 12, no. 9 (2012): 4960–4965, https://doi.org/10.1021/nl302560k.
36. K. Nath, A. Bin Rahaman, R. Moi, K. Maity, and K. Biradha, "Porous Li-Mof as a Solid-State Electrolyte: Exploration of Lithium Ion Conductivity through Bio-Inspired Ionic Channels," *Chem. Commun.* 56, no. 94 (2020): 14873–14876, https://doi.org/10.1039/d0cc05728b.
37. P. Butreddy, M. Wijesingha, S. Laws, G. Pathiraja, Y. Mo, and H. Rathnayake, "Insight into the Isoreticularity of Li-Mofs for the Design of Low-Density Solid and Quasi-Solid Electrolytes," *Chem. Mater.* 35, no. 23 (2023): 9857–9878, https://doi.org/10.1021/acs.chemmater.3c01021.
38. J. Liang, S. Qin, S. Luo, et al., "Epitaxially Growing Multilayer Coni-Mofs Nanosheets on Activated Carbon Cloth for High-Performance Asymmetric Supercapacitors," *J. Power Sources* 618 (2024): 235209, https://doi.org/10.1016/j.jpowsour.2024.235209.
39. X. Ma, J. Sha, B. Chen, et al., "Structurally Integrated 3d Vertically Porous Ni@Nio$_x$(Mno$_x$) Electrode for High-Performance Filter Electrochemical Capacitor," *Energy Storage Mater.* 75 (2025): 104083, https://doi.org/10.1016/j.ensm.2025.104083.
40. X. Li, G. Jiang, M. Jian, et al., "Construction of Angstrom-Scale Ion Channels with Versatile Pore Configurations and Sizes by Metal-Organic Frameworks," *Nat. Commun.* 14, no. 1 (2023): 286, https://doi.org/10.1038/s41467-023-35970-x.
41. M. Wang, L. Tong, S. Lv, et al., "In Situ-Engineered Mof/Polymer Hybrid Electrolyte with 3d Continuous Ion Channels for High-Voltage and Thermal-Resistant Lithium Metal Batteries," *Interdisciplinary Materials* 4, no. 5 (2025): 763–774, https://doi.org/10.1002/idm2.70005.
42. H. Bao, D. Chen, H. Ma, et al., "Engineering Ion Transport Highways through Polyoxometalate-Functionalized Metal–Organic Frameworks for Solid-State Lithium Batteries," *Adv. Funct. Mater.* 35, no. 47 (2025): 2505456, https://doi.org/10.1002/adfm.202505456.
43. D. Li, J. Wang, S. Guo, et al., "Molecular-Scale Interface Engineering of Metal–Organic Frameworks toward Ion Transport Enables High-Performance Solid Lithium Metal Battery," *Adv. Funct. Mater.* 30, no. 50 (2020): 2003945, https://doi.org/10.1002/adfm.202003945.

Supporting Information

Additional supporting information can be found online in the Supporting Information section.